

Compliant contact versus rigid contact: A comparison in the context of granular dynamicsArman Pazouki,^{1,*} Michał Kwartka,^{2,†} Kyle Williams,^{2,‡} William Likos,^{2,§} Radu Serban,^{2,||}
Paramsothy Jayakumar,^{3,¶} and Dan Negrut^{2,#}¹*Mechanical Engineering Department, California State University, Los Angeles, Los Angeles, California 90032, USA*²*College of Engineering, University of Wisconsin–Madison, Madison, Wisconsin 53706, USA*³*U.S. Army Tank Automotive Research, Development, and Engineering Center, Warren, Michigan 48397, USA*

(Received 4 April 2017; published 13 October 2017)

We summarize and numerically compare two approaches for modeling and simulating the dynamics of dry granular matter. The first one, the discrete-element method via penalty (DEM-P), is commonly used in the soft matter physics and geomechanics communities; it can be traced back to the work of Cundall and Strack [P. Cundall, *Proc. Symp. ISRM, Nancy, France* **1**, 129 (1971); P. Cundall and O. Strack, *Geotechnique* **29**, 47 (1979)]. The second approach, the discrete-element method via complementarity (DEM-C), considers the grains perfectly rigid and enforces nonpenetration via complementarity conditions; it is commonly used in robotics and computer graphics applications and had two strong promoters in Moreau and Jean [J. J. Moreau, in *Nonsmooth Mechanics and Applications*, edited by J. J. Moreau and P. D. Panagiotopoulos (Springer, Berlin, 1988), pp. 1–82; J. J. Moreau and M. Jean, *Proceedings of the Third Biennial Joint Conference on Engineering Systems and Analysis, Montpellier, France, 1996*, pp. 201–208]. The DEM-P and DEM-C are manifestly unlike each other: They use different (i) approaches to model the frictional contact problem, (ii) sets of model parameters to capture the physics of interest, and (iii) classes of numerical methods to solve the differential equations that govern the dynamics of the granular material. Herein, we report numerical results for five experiments: shock wave propagation, cone penetration, direct shear, triaxial loading, and hopper flow, which we use to compare the DEM-P and DEM-C solutions. This exercise helps us reach two conclusions. First, both the DEM-P and DEM-C are predictive, i.e., they predict well the macroscale emergent behavior by capturing the dynamics at the microscale. Second, there are classes of problems for which one of the methods has an advantage. Unlike the DEM-P, the DEM-C cannot capture shock-wave propagation through granular media. However, the DEM-C is proficient at handling arbitrary grain geometries and solves, at large integration step sizes, smaller problems, i.e., containing thousands of elements, very effectively. The DEM-P vs DEM-C comparison is carried out using a public-domain, open-source software package; the models used are available online.

DOI: [10.1103/PhysRevE.96.042905](https://doi.org/10.1103/PhysRevE.96.042905)**I. METHOD SUMMARY**

The dynamics of articulated systems composed of rigid and flexible bodies is characterized by a system of index-3 differential algebraic equations [1,2]

$$\dot{\mathbf{q}} = \mathbf{L}(\mathbf{q})\mathbf{v}, \quad (1a)$$

$$\mathbf{g}(\mathbf{q}, t) = \mathbf{0}, \quad (1b)$$

$$\mathbf{M}(\mathbf{q})\dot{\mathbf{v}} = \mathbf{f}(t, \mathbf{q}, \mathbf{v}) + \mathbf{G}(\mathbf{q}, t)\hat{\lambda}. \quad (1c)$$

The differential equation (1a) relates the time derivative of the generalized positions \mathbf{q} and velocities \mathbf{v} through a linear transformation defined by $\mathbf{L}(\mathbf{q})$. The presence of articulations, i.e., mechanical joints that restrict the relative motion of bodies in the system, leads in Eq. (1b) to a set of nonlinear kinematic constraint equations that must be satisfied by the generalized

coordinates \mathbf{q} . Finally, the force balance equation (1c) ties the inertial forces to the applied and constraint forces $\mathbf{f}(t, \mathbf{q}, \mathbf{v})$ and $\mathbf{G}(\mathbf{q}, t)\hat{\lambda}$, respectively. The expression of the constraint force projection operator \mathbf{G} is dictated by the nature of the articulations in the system, i.e., expression of $\mathbf{g}(\mathbf{q}, t)$ [1].

Granular, many-body, or discrete-element problems lead to large sets of generalized coordinates \mathbf{q} . For instance, granular flow in a hopper leads to 10^6 – 10^9 of entries in \mathbf{q} . Problems this large are ubiquitous; after all, as pointed out in [3], more than 50% of the materials processed in industry come in granular form. Understanding their dynamics is relevant in a range of practical applications such as additive manufacturing, terramechanics, nanoparticle self-assembly, composite materials, pyroclastic flows, formation of asteroids and planets, and meteorite cratering and also in industries such as pharmaceuticals, chemical and biological engineering, food processing, farming, manufacturing, construction, and mining. Note that granular dynamics does not occur only at the microscales or mesoscales. Avalanche dynamics and planet formation involve large bodies yet they qualify as granular dynamic ones, i.e., problems in which large collections of bodies mutually interact through friction and contact forces and have their motion modulated by their individual shape. Against this backdrop, the goal of this paper is to compare two methods, the discrete-element method via penalty (DEM-P) and the discrete-element method via complementarity

* apazouk@calstatela.edu

† kwarta@wisc.edu

‡ williams28@wisc.edu

§ likos@wisc.edu

|| serban@wisc.edu

¶ paramsothy.jayakumar.civ@mail.mil

Corresponding author: negrut@wisc.edu

(DEM-C), in relation to their performance in the context of solving the granular dynamics problem.

Mutual contact and ensuing friction can be accounted for in at least two ways, via a penalty approach or within a differential variational framework that invokes complementarity conditions. In the context of granular dynamics, we use the DEM-P to refer to the class of solution methods based on the penalty approach; we use the DEM-C to refer to the class of complementarity-based solutions. The DEM-P is a regularization method that relies on a relaxation of the rigid-body assumption [4–13]. It assumes that the bodies deform just slightly at the contact point. Employing the finite-element method to characterize this deformation would incur a stiff computational cost. Therefore, at each time step, a surrogate deformation of two bodies in mutual contact is generated during the collision detection stage of the solution by relying on the amount of interpenetration between bodies and also their shapes. Although the shapes might be overly complex, it is customary to combine the surrogate deformation with the Hertzian theory, which is only applicable for a handful of simple scenarios such as sphere-to-sphere or sphere-to-plane contact (see, for instance, [6]) in order to yield a general methodology for computing the normal (F_n) and tangential (F_t) forces at the contact point. As an example, a viscoelastic model based on Hertzian contact theory takes the form

$$F_n = \sqrt{\bar{R}\delta_n}(K_n\delta_n - C_n\bar{m}\mathbf{v}_n), \quad (2a)$$

$$F_t = \sqrt{\bar{R}\delta_n}(-K_t\delta_t - C_t\bar{m}\mathbf{v}_t) \quad (2b)$$

in normal n and tangential t directions, respectively. Herein, δ is the overlap of two interacting bodies, \bar{R} and \bar{m} represent the effective radius of curvature and mass, respectively, and \mathbf{v} is the relative velocity at the contact point [14]. For the materials in contact, the normal and tangential stiffness and damping coefficients K_n , K_t , C_n , and C_t are obtained, through various constitutive laws, from physically measurable quantities, such as Young's modulus, Poisson ratio, and the coefficient of restitution [6,15]. For granular dynamics via the DEM-P, the equations of motion need not be changed. Indeed, F_n and F_t are treated as any external forces and factored in the momentum balance of Eq. (1c) via $\mathbf{f}(t, \mathbf{q}, \mathbf{v})$. The specific DEM-P implementation used herein is detailed in [16].

The DEM-P is used widely in soft matter physics and geomechanics due to several attractive attributes, e.g., a large body of literature provides guidance via documented successful previous use, handling of friction and contact does not lead to any increase in numerical problem size, and the algorithm is simple with straightforward software implementation. The DEM-P has several drawbacks, e.g., identifying model parameters can be challenging, particularly for large heterogeneous granular systems; integration time steps are small owing to large values of the contact stiffness coefficients; proper friction force evaluation calls for maintaining a history of local tangential deformation (creep) for each contact (see [16]); and difficulties in handling contact for bodies of complex shapes, when the sphere-to-sphere or sphere-to-plane contact assumption that anchors the DEM-P is violated and the user has to fall back on *ad hoc* solutions to producing, for instance, suitable \bar{R} and \bar{m} values.

The DEM-C takes a different tack; it draws on a complementarity condition that imposes a nonpenetration unilateral constraint [see Eq. (3a)]. That is, for a potential contact i in the active contact set $\mathcal{A}(\mathbf{q}(t))$, either the gap Φ_i between two geometries is zero and consequently the normal contact force $\hat{\gamma}_{i,n}$ is greater than zero, or vice versa. The Coulomb friction model is posed via a maximum dissipation principle [17], which for contact i involves the friction force components $(\bar{\gamma}_{i,w}, \bar{\gamma}_{i,u})$ and the relative motion of the two bodies in contact [see Eq. (3b)]. The frictional contact force associated with contact i leads to a set of generalized forces, shown with an underbracket in Eq. (3c), which are obtained using the projectors $\mathbf{D}_{i,n}$, $\mathbf{D}_{i,u}$, and $\mathbf{D}_{i,w}$ (see, for instance, [18]). This leads in Eq. (3) to a so-called differential variational inequality problem [17]

$$0 \leq \Phi_i(\mathbf{q}) \perp \hat{\gamma}_{i,n} \geq 0, \quad (3a)$$

$$(\hat{\gamma}_{i,u}, \hat{\gamma}_{i,w}) = \arg \min_{\sqrt{\bar{\gamma}_{i,u}^2 + \bar{\gamma}_{i,w}^2} \leq \mu_i \hat{\gamma}_{i,n}} \mathbf{v}^T (\bar{\gamma}_{i,u} \mathbf{D}_{i,u} + \bar{\gamma}_{i,w} \mathbf{D}_{i,w}), \quad (3b)$$

$$\mathbf{M}(\mathbf{q})\dot{\mathbf{v}} = \mathbf{f}(t, \mathbf{q}, \mathbf{v}) + \mathbf{G}(\mathbf{q}, t)\hat{\lambda} + \sum_{i \in \mathcal{A}(\mathbf{q})} \underbrace{(\hat{\gamma}_{i,n} \mathbf{D}_{i,n} + \hat{\gamma}_{i,u} \mathbf{D}_{i,u} + \hat{\gamma}_{i,w} \mathbf{D}_{i,w})}_{i\text{th frictional contact force}}. \quad (3c)$$

Equations (3) are augmented with the kinematic differential equations and the set of bilateral constraint equations in Eqs. (1a) and (1b), respectively. The numerical solution of the resulting problem is challenging and continues to be an area of active research. Several numerical discretization approaches are discussed in [19–24]. The one adopted here was introduced in [25]; see also [18]. Upon time discretization followed by a relaxation of the kinematic constraints, the numerical problem is posed as a conically constrained quadratic optimization problem

$$\min_{\mathbf{q}(\gamma)} = \frac{1}{2} \gamma^T \mathbf{N} \gamma + \mathbf{p}^T \gamma, \quad (4a)$$

$$\text{subject to } \gamma_i \in \Upsilon_i \quad \text{for } i = 1, 2, \dots, n_c, \quad (4b)$$

where n_c is the number of active contacts, i.e., the number of elements in $\mathcal{A}(\mathbf{q}(t))$, Υ_i is the friction cone of contact i , $\gamma \equiv [\gamma_1^T, \gamma_2^T, \dots, \gamma_{n_c}^T]^T$, and $\gamma_i \equiv [h\bar{\gamma}_{i,n}, h\bar{\gamma}_{i,w}, h\bar{\gamma}_{i,u}]^T \in \mathbb{R}^3$, with h the simulation time step. The vector $\mathbf{p} \in \mathbb{R}^{3n_c}$ and positive-semidefinite matrix $\mathbf{N} \in \mathbb{R}^{3n_c \times 3n_c}$ change from time step to time step but do not depend on the Lagrange multipliers γ . The expressions of \mathbf{p} and \mathbf{N} , along with a detailed account of how the differential variational inequality problem stated in Eq. (3) leads to the conic constraint optimization problem in Eq. (4), can be found in [18]. We solve the optimization problem in Eq. (4) using Barzilai-Borwein or Nesterov algorithms [26,27]. This step represents the computational bottleneck of the DEM-C. Once the frictional contact forces γ are available, the velocity $\mathbf{v}^{(l+1)}$ is expeditiously computed using Eq. (3c). Subsequently, a half-implicit symplectic Euler scheme updates the positions at $t^{(l+1)}$, $\mathbf{q}^{(l+1)} = \mathbf{q}^{(l)} + h\mathbf{L}(\mathbf{q}^{(l)})\mathbf{v}^{(l+1)}$, and the solution is advanced by a time step h .

The DEM-C solution outlined has several advantages: It requires a small set of parameters, i.e., friction and cohesion coefficients, the simulation time step h can be large since there is no stiffness relied upon in the model, and the approach

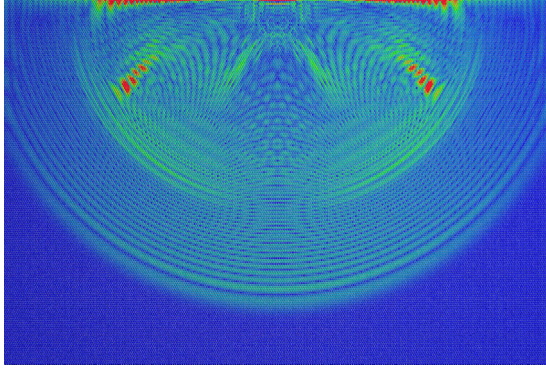


FIG. 1. Snapshot of the DEM-P wave propagation in granular media.

is suitable for handling bodies of arbitrary geometry. On the downside, the DEM-C requires at each time step the solution of an optimization problem, augments the size of the original problem as it introduces three additional unknowns ($\gamma_{i,n}, \gamma_{i,w}, \gamma_{i,u}$) for each active contact, which might be problematic for granular dynamics problems, and, owing to the positive-semidefinite attribute of \mathbf{N} , the convex optimization problem does not have a unique global solution. That is, multiple force distributions can solve the problem in Eq. (4). For the frictionless case, it can be proved that any of these distributions leads to the same particle velocities [25]. A recent result claims that the presence of friction does not alter this velocity uniqueness trait [28].

The DEM-P and DEM-C are very unlike each other as proved by their respective (i) local vs global takes on the frictional contact problem, (ii) deformable vs rigid-body perspectives, and (iii) force-acceleration vs impulse-momentum formulations. For (i), the DEM-C solves a coupled optimization problem that keeps with the global, or nonlocal, nature of the granular dynamics problem. Indeed, each contact influences all the rest as demonstrated by the system-level optimization problem of Eq. (4). Finally, from a numerical method perspective, the DEM-C “smooths” the discontinuity in forces and accelerations by operating with their time integrals: impulses and momenta.

II. NUMERICAL EXPERIMENTS

For the purpose of quantifying the accuracy, robustness, and efficiency of the DEM-P and DEM-C we use an open source simulation infrastructure that implements both approaches. This simulation engine is called CHRONO [29,30] and it is used here for a wave propagation experiment, a cone penetration test, a direct shear test, a triaxial test, and a hopper flow analysis. The metrics of interest in this DEM-P vs DEM-C comparison are solution accuracy, robustness, and required computational effort as reflected in simulation run-times.

A. Wave propagation in granular material

The propagation of a wave in granular material (see the DEM-P simulation snapshot in Fig. 1) is the result of inter-particle energy exchange via impact, contact, and adhesion. In the DEM-P results reported herein, these interactions

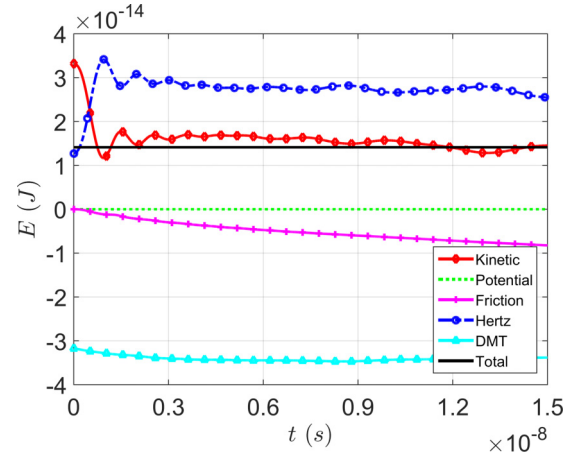


FIG. 2. The DEM-P wave propagation simulation: balance of total energy E over time. The Coulomb friction coefficient $\mu = 0.18$. The total energy was computed as $E = K - U - E_I - W_f - E_A$. Impact, contact, and adhesion are represented using the Hertz, Mindlin, and Derjaguin-Muller-Toporov (DMT) models, respectively [6,31].

were captured by the Hertz, Mindlin, and Derjaguin-Muller-Toporov models [6,31]. The sensitivity of the solution to noise, particularly in nonlinear regimes caused by larger impact velocities, demands a nondissipative and nongenerative numerical solution. We monitor energy conservation for an experimental setup composed of a collection of n monodisperse spheres of diameter $d = 1.08 \mu\text{m}$, which were disposed in one layer with close packing. The material properties used were Young’s modulus $Y = 78 \text{ GPa}$, Poisson’s ratio $\nu = 0.17$, and friction coefficient $\mu = 0.18$. In simulation, we assign an initial velocity to one surface particle and subsequently monitor the wave propagation.

Numerical experiments were carried out for different values of bodies $n_B \in [0.4, 120] \times 10^3$ and impact velocity $v \in [0.1, 10] \text{ m/s}$. The DEM-P simulation lasted for one wave sweep of the domain, which had a 3:4 aspect ratio; i.e., for instance, for $n_B = 120\,000$, the domain’s height and width were 300 and 400 particles, respectively. Figure 2 illustrates the variation of the energy components over time, as well as the variation of the total energy E , defined as $E = K - U - E_I - W_f - E_A$, where K , U , E_I , W_f , and E_A denote the kinetic energy, gravity potential, impact energy, work of the shear force, and adhesion energy, respectively. The solution accuracy metric was the variation in total energy $e = (E_f - E_i)/K_i$, where subscripts f and i denote the final and initial states. Regardless of n_B and impact velocity v , we noticed that $e < 10^{-6}$. Note that combining the complementarity approach with the rigid-body model yields a solution incapable of simulating wave propagation. As such, there are no DEM-C results to report. A finite-element method take on grain deformation, i.e., relaxing the rigid-body assumption, would address this issue, albeit at a steep computational cost.

B. Cone penetration

In this section we report laboratory and simulation tests performed for a cone penetration experiment. This

TABLE I. Properties of cones.

Property	Cone	
	30°	60°
length L (mm)	34.36	22.10
width W (mm)	9.21	19.86
total mass with LVDT attached m (g)	141.1	135.7
Young's modulus Y (GPa)	193	193
Poisson's ratio ν	0.3–0.31	0.3–0.31

geomechanics soil characterization method uses a standardized cone geometry, material, bucket dimension, and granular material compaction. With few exceptions noted in [32], the procedure and equipment used in this test were as in the British and Swedish standards [33]. The cones, which had apex angles of 30° and 60° in line with the British and Swedish standards, respectively, have the geometric and mechanical properties provided in Table I.

The cones were dropped from three heights: from a height equal to the cone's length ($L_{30^\circ} = 34.36$ mm and $L_{60^\circ} = 22.10$ mm), a half-cone height ($\frac{1}{2}L_{30^\circ} = 17.18$ mm and $\frac{1}{2}L_{60^\circ} = 11.05$ mm), followed by a zero height, where the cone was placed right above the specimen's surface (see Fig. 3). The cones were attached to brass adapters to facilitate connection to a linear variable differential transformer (LVDT) rod [see Fig. 4(c)], which was used to measure the displacement of the cones during penetration. The falling cones were attached to an adjustable vertical stand as illustrated in Fig. 4(d). The vertical stand had a range of 0.4 m that allowed the LVDT rod and fall cones to drop into the center of 4- or 6-in. proctor molds, as specified in the ASTM D698 standard. The granular material used was monodisperse glass beads. A size characterization using the MATLAB® image processing toolbox was conducted to quantify bead shape. The bead's average diameter and standard deviation were measured as 2.849 and 0.0417 mm, respectively.

Two material compactations were considered, one loose and one dense. In the laboratory, the loose compaction was

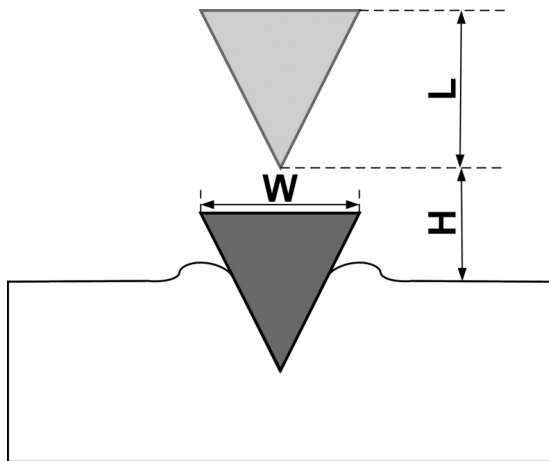


FIG. 3. Schematic of a cone drop experiment, with drop height H , cone height L , and cone width W .

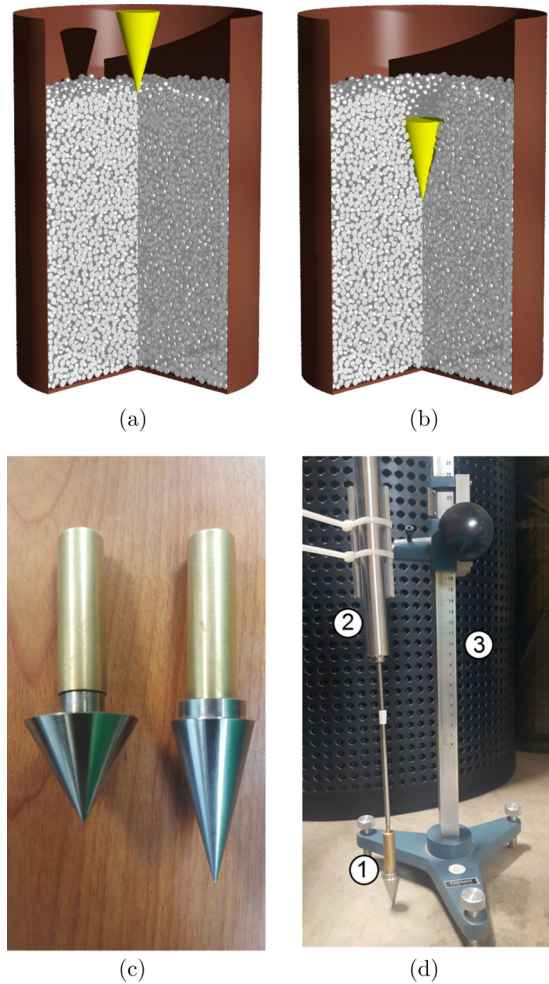


FIG. 4. Empirical and numerical cone penetration setups showing (a) a cone placed over the settled specimen, (b) a cone penetrating the granular material, (c) fall cones with LVDT connectors, and (d) a view of the assembled apparatus: 1, fall cone and adapter; 2, LVDT; and 3, adjustable vertical stand.

generated by placing the material in accordance with ASTM D5254. For dense compaction, the material was placed in lifts. After each lift, an extrusion plate was placed onto the material. The center of the extrusion plate was then hit with a standard proctor hammer ten times. This was repeated for a total of four lifts. On the simulation side, the granular material at rest was generated by pouring particles into the container with and without friction to generate the loose and dense setups, respectively. For the DEM-P, the following parameters were used for the grains and container: Young's modulus $Y = 10^8$ Pa (the material was softer than in reality to allow for large step sizes h), Poisson's ratio $\nu = 0.3$, and the beads' density $\rho = 2500$ kg/m³. For both the DEM-P and DEM-C, $\mu_{p-p} = \mu_{c-p} = 0.7$, where c stands for cone and p for particle (bead). These μ values are within the range recommended in the literature (see the discussion in [34]). Given the nature of the material considered, we used the same μ value also for the direct shear test in Sec. II C and the hopper experiment in Sec. II E. Loose and dense compaction densities obtained are provided in Tables II and III.

TABLE II. Void ratios at rest.

Scenario	Experiment	Simulation [relative error (%)]	
		DEM-P	DEM-C
Container of 4-in. diameter			
loose case	0.66	0.72 (9.50)	0.75 (13.79)
dense case	0.53	0.55 (3.85)	0.57 (6.61)
Container of 6-in. diameter			
loose case	0.66	0.71 (7.15)	0.74 (12.43)
dense case	0.53	0.55 (3.46)	0.56 (5.23)

With the exception of Young’s modulus Y , all parameter values were lifted from the literature based on the materials involved in the experiment. However, we had to perform one calibration step that complemented the choice of parameter values. The motion of the LVDT rod was modeled in CHRONO by a perfect, i.e., frictionless, translational joint that constrained the cone to move only in the vertical direction. This amounted to the presence of five kinematic constraints [see Eq. (1b)]. We performed laboratory fall tests in the absence of granular material to quantify the actual friction between the fall cone and the adapter. We measured that the friction in the laboratory apparatus led to free fall speeds at impact that would require $[0.65, 0.94]g$ [32], where $g = 9.81 \text{ m/s}^2$. The outcome of this calibration phase was that in simulation, we used a gravitational acceleration of $0.79g$ to account for the net effect of friction in the apparatus, friction that was otherwise neglected by the CHRONO-idealized translational joint.

The cone penetration simulations consisted of two stages. In the first stage (settling), granular material was dropped into the container. Although this stage was 1.0 s long, a suitable rest state, as measured by the value of kinetic energy associated with the movement of all elements, was reached after approximately 0.5 s (see Fig. 5). In the second stage (cone falling), the cone dropped and penetrated the granular material over 0.4 s. The vertical displacement of the cones as a function of time is presented in Fig. 6. Four different scenarios are shown for 4- and 6-in.-wide containers, 30° and 60° fall cones, and loose and dense compaction.

Overall, the DEM-P and DEM-C results are very comparable and the methods are deemed predictive. Generally, the DEM-P and DEM-C simulation penetration depths were within 12% of laboratory measurements in all scenarios (see Table IV). The DEM-P produced more accurate results for the settling phase; for the penetration phase, the DEM-C

TABLE III. Densities at rest (kg/m^3).

Scenario	Expt.	Simulation [relative error (%)]	
		DEM-P	DEM-C
Container of 4-in. diameter			
loose case	1504.29	1449.50 (3.64)	1426.00 (5.20)
dense case	1630.34	1608.79 (1.32)	1593.69 (2.25)
Container of 6-in. diameter			
loose case	1504.32	1462.70 (2.77)	1433.39 (4.72)
dense case	1630.35	1610.93 (1.19)	1601.22 (1.79)

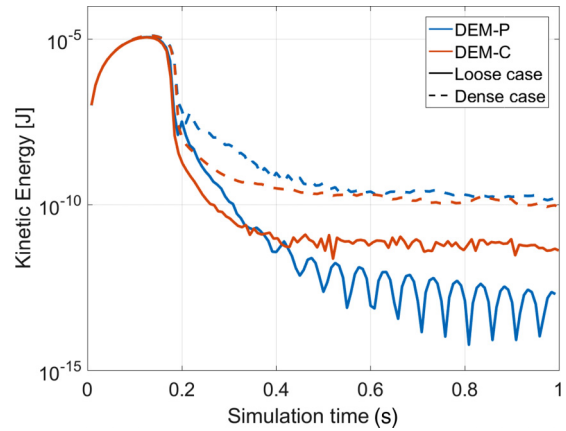


FIG. 5. Evolution of the system’s kinetic energy (on a lin-log scale) during the first, i.e., settling, stage of the simulation.

produced slightly more accurate results for the loose case. On average, when using CHRONO, the DEM-C was about 1.6 times slower than DEM-P (see Table V). The table reports run-time ratios $T_{\text{DEM-C}}/T_{\text{DEM-P}}$ for times required to complete the cone penetration simulations. In the column headings, 4 and 6 represent the cylinder diameter in inches, while L and D stand for loose and dense packing, respectively. In the first column, settling, penetration, and total refer to the stages of the simulation: settling phase, material penetration phase, and total run-time. The very last row reports the number of elements used to fill the container in each scenario. As expected, the dense-packing cases have more elements compared to the loose-packing cases. Further numerical results are available in [34].

C. Direct shear test with particle image velocimetry

The direct shear test for granular materials is often used in geomechanics to infer friction angles. The shear box, which is divided horizontally, is filled with material at a desired density. A normal force is applied to the top of the sheared material; a tightly controlled motion causes half of the shear box to slide laterally, causing shear forces to develop in the sample. This setup was modified to allow the tracking of individual grains via particle image velocimetry (PIV) as enabled by the GEOPIV software [35]. To this end, the shear box had a transparent front wall for capturing the glass beads’ movement with a digital camera. The moving portion of the shear box was displaced at a constant rate using a GeoTAC GeoJac stepper motor controlled with the GeoTAC Sigma-1 loading software. The forces required to move the box and sample were measured using an Interface ULC Ultra Low Capacity Load Cell model ULC-2N. The motor frame and shear box are shown in Fig. 7 (see also [36]).

The material and parts were dry; two shear rates were considered separately: 0.5 and 1.0 mm/min. The normal force on the shear plane was controlled by inclining the shear apparatus and adding, in a tightly controlled fashion, a supplemental mass on top of the material. The apparatus was inclined at 18° with no supplemental mass, 24° with 8.01 g of additional mass, and, for 30° , 53.64 g for 1.0 mm/min and 66.64 g for 0.5 mm/min. The tests were conducted using

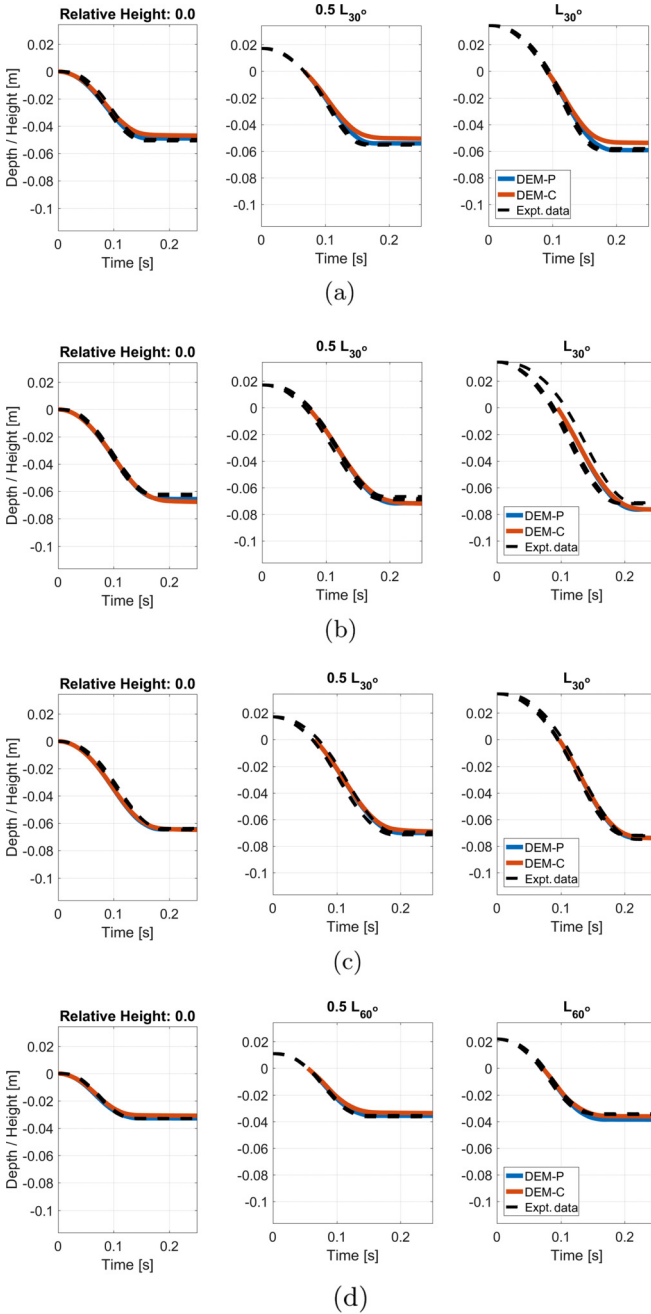


FIG. 6. Cone depth vs time plots obtained from simulation and laboratory experiments: (a) cone 30° in apex angle, container with a 6-in.-wide diameter, and dense packing; (b) cone 30° in apex angle, container with a 6-in.-wide diameter, and loose packing; (c) cone 30° in apex angle, container with a 4-in.-wide diameter, and loose packing; and (d) cone 60° in apex angle, container with a 6-in.-wide diameter, and dense packing. Black lines indicate experimental data, blue is used for DEM-P results and orange is for DEM-C results. In several cases the blue line is right behind the orange line.

granular material in two different compactations, loose and dense. In the dense case between 1303 and 1310 elements were arranged in one layer via hexagonally close packing. In the loose case the shear box was filled out with 1174–1214 elements under arbitrary packing (see Fig. 8). The simulations consisted of 1311 (dense) and 1154 (loose case)

TABLE IV. Cone penetration results related to plots in Fig. 6. Four different scenarios were classified by container diameter ϕ , cone apex angle ψ , and material compaction C for triple (ϕ, ψ, C) values: (a) (6 in., 30°, D), (b) (6 in., 30°, L), (c) (4 in., 30°, L), and (d) (6 in., 60°, D), where L and D stand for loose and dense compaction, respectively.

Scenario	Initial height	Depth (cm) [relative error (%)]		
		Laboratory	DEM-P	DEM-C
(a)	0	5.01	4.90 (2.34)	4.73 (3.31)
(a)	$\frac{1}{2}L_{30^\circ}$	5.49	5.42 (1.35)	5.11 (5.62)
(a)	L_{30°	5.86	5.92 (1.09)	5.44 (8.17)
(b)	0	6.25	6.56 (4.84)	6.84 (4.34)
(b)	$\frac{1}{2}L_{30^\circ}$	6.79	7.17 (5.59)	7.29 (1.62)
(b)	L_{30°	7.17	7.63 (6.34)	7.73 (1.33)
(c)	0	6.43	6.45 (0.19)	6.57 (1.95)
(c)	$\frac{1}{2}L_{30^\circ}$	7.04	7.01 (0.32)	7.01 (0.10)
(c)	L_{30°	7.30	7.38 (1.08)	7.52 (1.92)
(d)	0	3.29	3.28 (0.36)	3.11 (4.96)
(d)	$\frac{1}{2}L_{60^\circ}$	3.59	3.56 (0.63)	3.40 (4.61)
(d)	L_{60°	3.44	3.85 (11.80)	3.64 (5.49)

glass spheres of diameter 2.84 mm. For the DEM-P, the density $\rho = 2500 \text{ kg/m}^3$, Young’s modulus $Y = 50 \text{ GPa}$, Poisson’s ratio $\nu = 0.3$, the coefficient of restitution $c_r = 0.66$, and the intersphere coefficient of friction $\mu = 0.7$. The DEM-C used only the aforementioned density and friction values. The shear box was 101.96 mm wide and the depth of its fixed half was 50.58 mm. The distance between the front and back panels was 3.3 mm.

Insofar as the simulation experiments were concerned, a sensitivity analysis was first conducted with respect to the shearing speed V_{sh} . The shear speeds in the laboratory were low and led to lengthy experiments that needed to be duplicated in simulation. We ran one pilot DEM-C simulation in CHRONO using the actual laboratory shearing speed. When using one thread on an i5-4300M CPU @ 2.0 GHz processor, the simulation finished after 23 days. The DEM-P would have required close to 54 days. The purpose of the sensitivity analysis was to understand whether increasing the shear speed in the simulation would significantly alter the results. A thorough account of this study is provided in [36]. Both the DEM-P and DEM-C show little sensitivity to shearing speed. Due to the long execution times, the DEM-P simulations run had $V_{sh,sim} \geq 4 \text{ mm/min}$, i.e., at least four times faster than

TABLE V. Run-time ratios T_{DEM-C}/T_{DEM-P} and number of elements in the cylinder. In the column headings, 4 and 6 represent the cylinder diameter in inches, while L and D stand for loose and dense packing, respectively.

Stage	4L	4D	6L	6D
settling	1.54	1.67	1.46	1.44
penetration	1.64	1.76	1.78	1.71
total	1.56	1.69	1.58	1.55
num. elements	48864	53296	110786	120860



FIG. 7. Shear apparatus: 1, sliding portion of the shear box; 2, fixed portion of the shear box; and 3, load cell.

experiment. The trajectories obtained from those simulations were very similar to each other (see Fig. 9). The DEM-C simulations were two to six times faster than DEM-P simulations; all were carried out in CHRONO. Different values of V_{sh} did not lead to consequential changes in numerical values reported. Surprisingly, we observed a slightly better match of the DEM-C numerical and experimental results for higher shearing velocities, an artifact that might be related to the particular solution approach used in CHRONO [27,37,38].

Particle arrangements at the end of the laboratory and simulation tests are shown in Fig. 8. The laboratory PIV and simulation trajectories are juxtaposed in Fig. 9. The spheres marked on the plots show the positions of the monitored particles at the beginning of the test. Six experiments, three different incline angles at two shearing speeds, were run for loose and then dense compaction for a total of 12 scenarios. Except for a small number of scenarios in the close-packed

configurations, the results are in good agreement for the duration of the motion. We observed that in the laboratory dense-packed scenarios, generating a perfectly closed initial configuration was almost impossible due to the presence of small voids caused by particle imperfection and shear box dimensional tolerances. The existence of clearances in the loose case initial configuration was noted for significantly influencing particle motion.

Note that it was not possible to exactly match the initial locations of the experiment vs simulation spheres. Indeed, at time $t = 0$, the physical experiment and numerical simulation rest configurations were slightly different. This difference in initial conditions was reconciled by comparing the trajectories of six reference spheres in the physical experiment to those of six simulation spheres that were closest to the reference spheres at the onset of the shearing process [36]. The simulation spheres monitored are marked in red in Fig. 8. This sphere selection process was followed to generate all results reported in Fig. 9.

D. Triaxial test

For the standard triaxial test (STT), we summarize the comparison of DEM-P and DEM-C results against experimental data reported in [39]. This discussion draws on simulation setup information and results provided in [40].

The experiment was conducted using a cylinder with diameter of 101 mm and height of 203 mm. Two specimen

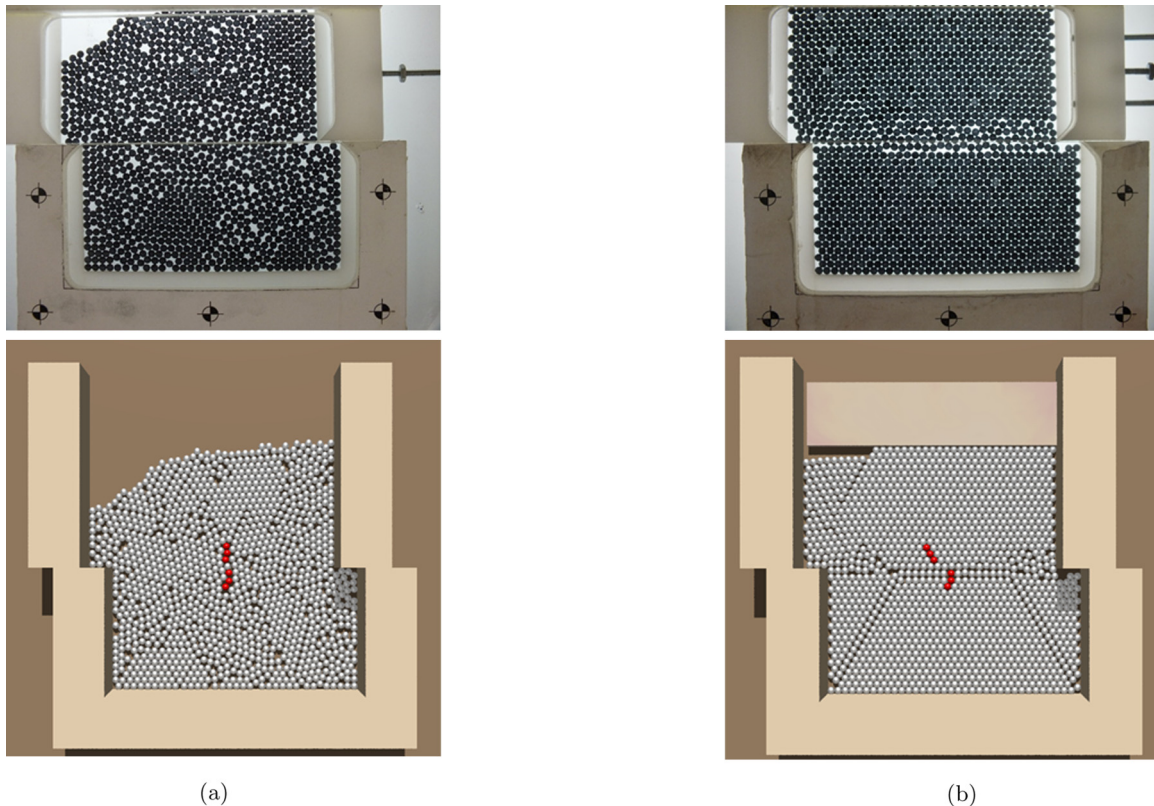


FIG. 8. Particle arrangement comparison at the end of the shear test for experiment (top) and simulation (bottom) with granular material (a) randomly packed loosely with an incline angle of 18° and a shearing speed of 1.0 mm/min and (b) hexagonally packed densely with an incline angle of 24° and a shearing speed of 0.5 mm/min. Six particles, marked in red, were selected for analyzes via PIV.

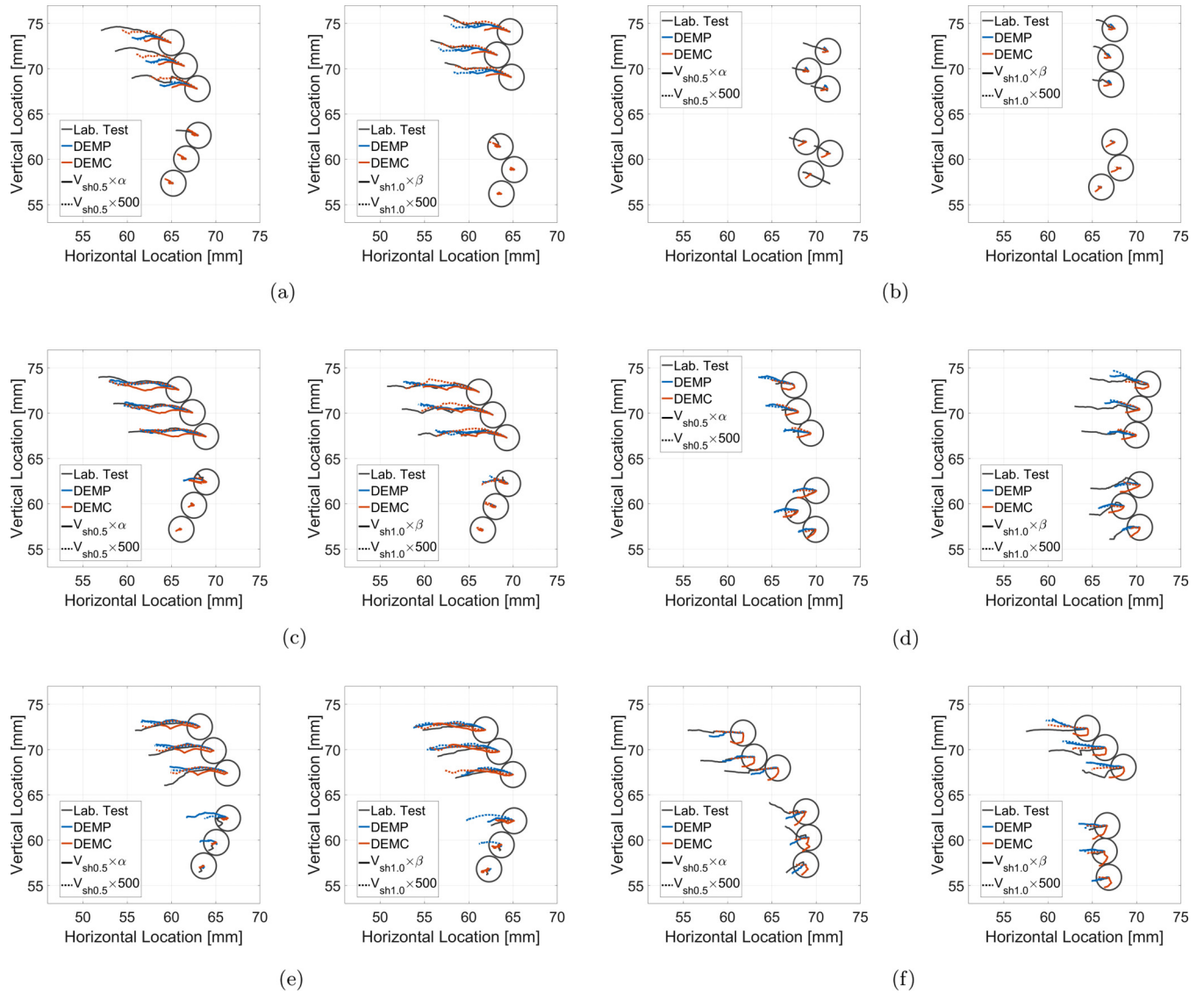


FIG. 9. Trajectories for selected particles obtained from simulation and laboratory experiments: (a) particles packed densely and the shear box inclined at 18° , (b) particles packed loosely and the shear box inclined at 18° , (c) particles packed densely and the shear box inclined at 24° , (d) particles packed loosely and the shear box inclined at 24° , (e) particles packed densely and the shear box inclined at 30° , and (f) particles packed loosely and the shear box inclined at 30° . Two plots are provided in (a)–(f); the left and right plots correspond to $V_{sh} = 0.5$ mm/min and $V_{sh} = 1.0$ mm/min, respectively. Two sets of trajectories obtained in simulations are shown. The first set presents the results with shearing velocity 500 times larger than the one used in laboratory ($V_{sh,sim} = V_{sh} \times 500$); these simulations are shown with dotted lines, which are always orange for the DEM-C and blue for the DEM-P. The second set of results, shown with solid lines, is obtained for shearing speeds closer to experiment; i.e., the speed-up factors α for $V_{sh} = 0.5$ mm/min and β for $V_{sh} = 1.0$ mm/min are both significantly less than 500. Since the DEM-P was slower, the slowest shearing velocities we simulated with were 4 mm/min, which gives $V_{sh,sim} = V_{sh0.5} \times 8$ and $V_{sh1.0} \times 4$, i.e., ($\alpha = 8, \beta = 4$). For the DEM-C, no shearing speed-up was needed in the simulation, i.e., $\alpha = \beta = 1$.

types were used. In the monodisperse case we used spheres of 5 mm diameter; in the polydisperse case we used a uniform mixture of spheres with diameters of 4, 5, and 6 mm. The beads were made of grade 25 chrome steel; the confining pressure was 8×10^4 Pa; the sample was compressed at an axial strain rate of $0.0083\% \text{ s}^{-1}$. In simulation, the following values were used by the DEM-P: density $\rho = 7800 \text{ kg/m}^3$, Young’s modulus $Y = 2 \times 10^8 \text{ Pa}$, Poisson ratio $\nu = 0.28$, and coefficient of restitution $c_r = 0.6$. The same values were used for the container’s walls. The particle-to-particle and particle-to-wall friction coefficients were measured in [41,42]:

0.096 and 0.28, respectively. The confining pressure was set to $8 \times 10^4 \text{ Pa}$. The DEM-C did not need values for Y , ν , and c_r . There were two caveats in simulating the STT. First, just like for the shear test, laboratory shearing speeds were too low to be matched in simulation, which was carried out after a three order of magnitude increase in strain rate to $10\% \text{ s}^{-1}$. Second, the material was softened by three orders of magnitude to allow for a larger DEM-P time step h . A sensitivity analysis suggests that the relaxation of test parameters changed neither the qualitative nor the quantitative outcomes of the study [40].

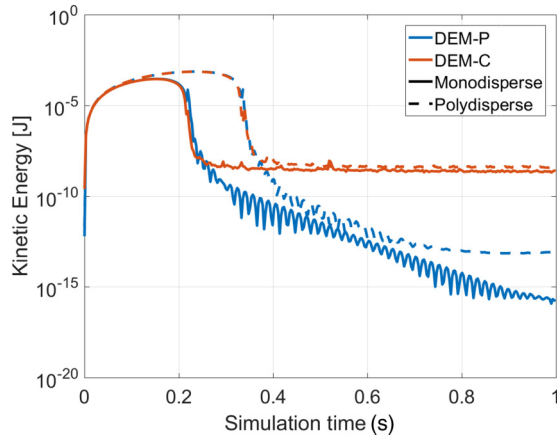


FIG. 10. Evolution of the system’s kinetic energy during the standard triaxial test settling stage.

The simulations consisted of two stages. In the settling stage, the specimen was poured into the container and the confining pressure was applied to its top and sidewalls to bring the sample to rest (see Fig. 10). In the second stage, the confining pressure of 8×10^4 Pa was maintained on the sidewalls and the axial strain rate was applied to the top wall. The bottom wall was fixed in both stages. The compressed specimen after the settling stage and after the STT is shown in Fig. 11.

The laboratory tests used between 15 382 and 15 420 spheres yielding void ratios of 0.615 and 0.612, respectively. The DEM-P and DEM-C used 15 918 spheres in the monodisperse case and 15 740 in the polydisperse case. The simulation void ratios at rest ranged from 0.611 to 0.660 (see Table VI).

To simulate the settling and the STT stages it took the DEM-P an average of 1 h 25 min and 4 h and 55 min, respectively. The DEM-C took 9 h 21 min for settling and 44 h and 14 min for the STT stage. Simulations were run using ten threads on an Intel i5-4300M CPU @ 2.0 GHz.

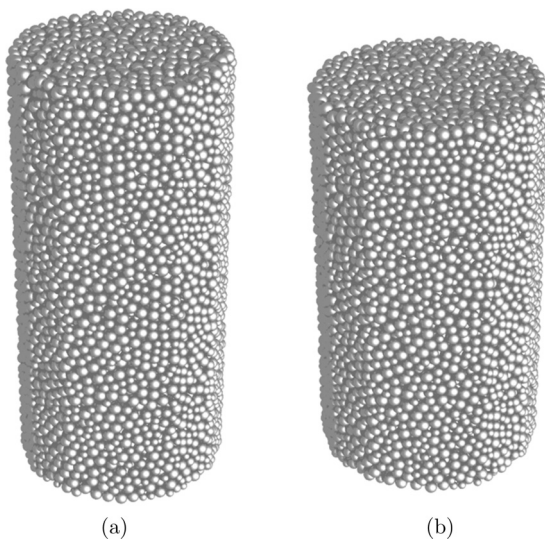


FIG. 11. Granular material simulation snapshot at the end of (a) the settling stage and (b) the standard triaxial test stage.

TABLE VI. Number of spheres used and void ratios obtained after the settling stage. Here mono. denotes the monodisperse case and poly. the polydisperse case.

Approach	Number of spheres	Void ratio [relative error range (%)]
Laboratory Expt.	(15382, 15420)	(0.615, 0.612)
mono. DEM-P	15918	0.641 ([4.06, 4.52])
mono. DEM-C	15918	0.611 ([0.65, 0.16])
poly. DEM-P	15740	0.660 ([6.82, 7.27])
poly. DEM-C	15740	0.626 ([1.76, 2.24])

A comparison of laboratory, DEM-P, and DEM-C results is provided in Fig. 12 (see also Table VII), in which the variation in stress ratio $(\sigma_1 - \sigma_3)/(\sigma_1 + \sigma_3)$ is plotted as a function of axial strain. The reference data are from [39]. Both the DEM-P and DEM-C match experimental data, particularly so at high axial strains. The DEM-C, which attempts to enforce the rigid-body abstraction, leads to a specimen that is perceived as stiffer, thus causing a steeper initial slope. The DEM-P provides a good approximation of the laboratory data at every stage of the experiment.

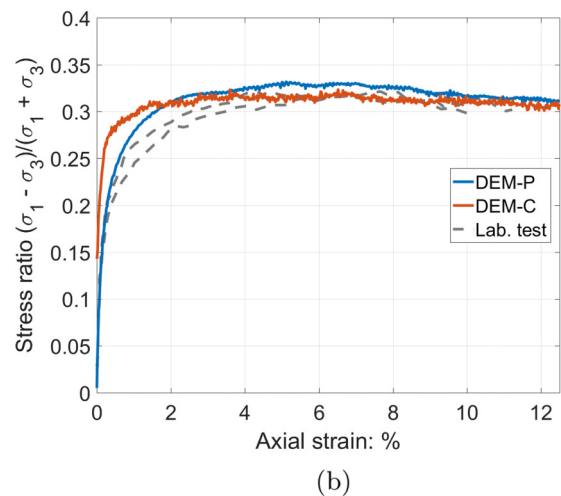
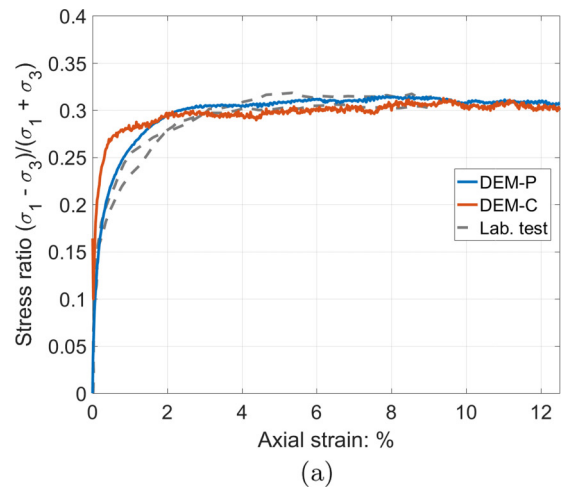


FIG. 12. Laboratory vs simulation results for the standard triaxial test with (a) a monodisperse specimen and (b) a polydisperse specimen.

TABLE VII. Summary of execution time for the standard triaxial test.

Approach	Length of time simulated (s)	Average exec. time
DEM-P	settling ≈ 0.5	1 h 25 min
DEM-P	STT 1.5	4 h 55 min
DEM-P	total ≈ 2.0	6 h 20 min
DEM-C	settling ≈ 0.5	9 h 21 min
DEM-C	STT 1.5	44 h 14 min
DEM-C	total ≈ 2.0	53 h 35 min

E. Flow sensitivity with respect to element shape

A hopper experiment provides an opportunity to scrutinize via fully resolved, microscale simulation emerging macroscale attributes such as flow rate, funnel flow, arching, interlocking, jamming, etc. We reported in [43] the outcome of a DEM-C sensitivity analysis of hopper flow rate with respect to friction coefficient. The hopper, which consisted of one 45° inclined and three vertical walls, was filled with approximately 40 000 glass disruptor beads with a 500 μm diameter. The same hopper setup is used herein (see Figs. 13 and 14). The material properties for the glass beads are those from the cone penetration and PIV tests; i.e., a single value of friction coefficient $\mu = 0.7$ was assumed for all contact events. Except for transitions at the onset and conclusion of the flow, we confirm the hour-glass principle that a monodisperse dry spherical-granular material flows uniformly throughout the entire process (see Table VIII). To obtain these values, if the duration of the granular flow through hopper was T_f , we split the time interval $[0.3, 0.9]T_f$ into ten equal-size subintervals. The average flow rate for each subinterval was calculated based on a linear regression of the flow-time data in that subinterval, yielding ten flow rates. The table reports flow rate average \dot{m} , standard deviation SD, and normalized standard deviation $\zeta = SD/\dot{m}$ obtained using these ten values.

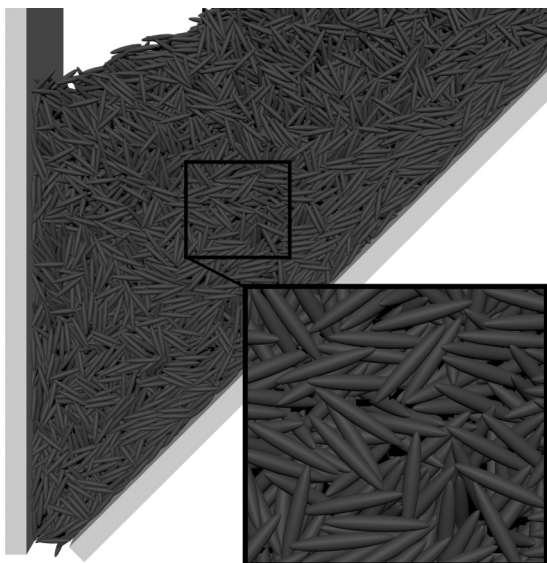


FIG. 13. Flow of prolate ellipsoid through a hopper with $\alpha = 3.4$.

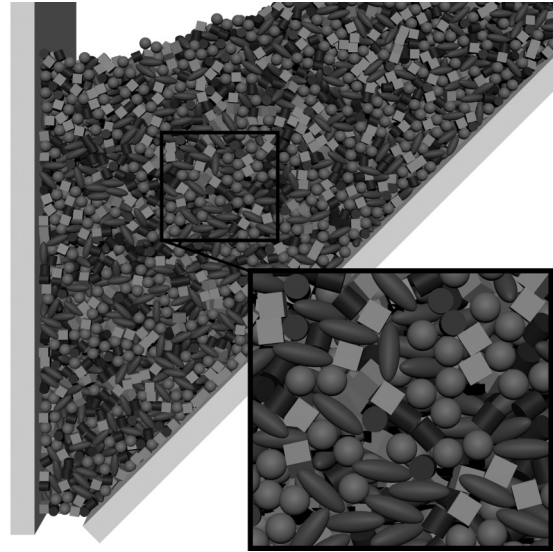


FIG. 14. Heterogeneous granular flow through a hopper. The material is composed of equal fraction of spheres, ellipsoids ($\alpha = 2$), boxes, and cylinders.

The results in Table IX answer the following question: How sensitive are the simulation results to decreasing Y in order to reduce simulation times via larger integration step sizes h ? It turns out that for the hopper experiment, one can reduce Y substantially without compromising the simulation results. In our experience, the extent to which one can reduce Y is problem dependent.

The DEM-P method, shown in Sec. II A to successfully capture nonlinear wave propagation, builds on the assumption that the contact scenarios encountered are of simple types such as sphere-to-sphere or sphere-to-plane contact scenarios. Then, insofar as the normal contact force is concerned, an analytical solution can be produced [6,44–46] in terms of quantities such as the effective radius of curvature \bar{R} , effective mass \bar{m} , and contact stiffness and damping parameters [see Eq. (2)]. Note that these sphere-to-sphere or sphere-to-plane contact geometries, which come into play when defining, for instance, \bar{R} and \bar{m} , allow also for a clean tracking of the contact history that comes into play in the computation of the DEM-P forces [16]. Yet practical applications oftentimes lead to edge-to-edge, corner-to-plane, edge-to-plane, etc., contact scenarios that bring together complex geometries of arbitrary size ratios and/or relative orientations. How should the DEM-P handle

TABLE VIII. Comparison of hopper flow rates for different gap sizes (in mm). Here \dot{m} and SD denote flow rate and standard deviation measured in g/s, respectively; ψ denotes the normalized standard deviation and $\zeta = SD/\dot{m}$.

Gap size	\dot{m} (SD, 100ζ)		
	Expt.	DEM-P	DEM-C
1.5	1.42	1.50 (0.10, 6.5)	1.48 (0.10, 6.7)
2.0	2.69	2.71 (0.09, 3.3)	2.80 (0.15, 5.3)
2.5	4.23	4.20 (0.08, 2.0)	4.28 (0.12, 2.7)

TABLE IX. The DEM-P sensitivity analysis with respect to the modulus of elasticity Y , measured in Pa. Here \dot{m} and SD denote flow rate and standard deviation measured in g/s, respectively; w is measured mm.

Y	\dot{m} (SD)		
	$w = 1.5$	$w = 2.0$	$w = 2.5$
6.0×10^6	1.48 (0.03)	2.72 (0.12)	4.22 (0.09)
2.5×10^7	1.49 (0.09)	2.72 (0.12)	4.21 (0.13)
1.0×10^8	1.53 (0.11)	2.71 (0.12)	4.18 (0.15)
4.0×10^8	1.46 (0.09)	2.74 (0.09)	4.21 (0.13)
1.6×10^9	1.50 (0.07)	2.75 (0.08)	4.24 (0.14)

these cases? Various computational geometry heuristics exist for producing surrogates for the contact point, normal contact direction, and relative penetration speed (see, for instance, [47–49]). Against this backdrop, one can regard the DEM-P as either an approach that considers elastic deformation and no penetration, with the frictional contact force modulated by geometric (\bar{R} and \bar{m}) and material (K_n , K_t , C_n , and C_t) parameters [see Eq. (2)] [6], or an *ad hoc* approach not concerned with the local elastic deformation but rather with the mutual penetration, in which case a penetration metric, e.g., the intersection volume for the two geometries in contact, and additional empirical parameters dictate the frictional contact force [47–49]. At the price of not being able to handle arbitrary geometries, we embrace the elastic deformation orthodoxy for the DEM-P and root the frictional contact force computation in an analytical argument as done in the Hertzian contact theory [6]. How well an empirical penetration-based DEM-P solution manages to capture nonlinear phenomena such as in Sec. II A and, at the same time, handle complex geometries falls outside the scope of this work.

The DEM-C does not face this conundrum, i.e., how complex geometry should be handled, as it always falls back on a unilateral (nonpenetration) kinematic constraint grafted onto the rigid-body model. For low-strain scenarios, such as hopper flow, the rigid-body assumption captures well the flow of the material (see results in Table VIII). This was the rationale for employing the DEM-C in a study that sought to quantify how shape dictates hopper flow. To this end, we considered six scenarios. In four cases, the granular material was composed of prolate ellipsoids. The elongation α was defined as the ratio of the larger to the smaller semiaxis. Figure 14 illustrates the hopper flow of prolate ellipsoids with $\alpha = 3.4$. In the fifth scenario, the granular material was composed of cubes. The sixth scenario included in equal amounts elements of four types: spheres, cubes, cylinders with equal height and diameter, and prolate ellipsoids with $\alpha = 2.0$ (see Fig. 13). Each particle’s volume was equal to that of a 500- μm -diam sphere. In all cases, the flow of granular material was approximately constant, but different from case to case (see Table X). Unsurprisingly, the more needlelike the prolate ellipsoids, the lower their flow rate. The cubes’ flow rate was low; “lubrication” via other geometries improved the granular mixture flow rate. No jamming was observed; nonetheless, compared to the spherical particles, the flow of nonspherical particles was more unpredictable

TABLE X. The DEM-C flow rate in the hopper for different mixtures and gap size w (mm). The flow rate \dot{m} and standard deviation SD are measured in g/s.

Granular composition	\dot{m} (SD)		
	$w = 1.5$	$w = 2.0$	$w = 2.5$
sphere ($\alpha = 1.0$)	1.60 (0.09)	2.87 (0.10)	4.42 (0.09)
prolate ellipsoid ($\alpha = 2.0$)	1.45 (0.10)	2.54 (0.14)	4.07 (0.21)
prolate ellipsoid ($\alpha = 3.0$)	1.00 (0.19)	2.20 (0.21)	3.33 (0.22)
prolate ellipsoid ($\alpha = 4.0$)	0.49 (0.11)	1.46 (0.33)	2.49 (0.26)
cube	0.58 (0.11)	1.96 (0.34)	3.28 (0.25)
mixture	1.14 (0.19)	2.25 (0.18)	3.59 (0.20)

(see standard deviation values). We also report the value of SD/\dot{m} in Table XI. This ratio, which can be interpreted as a propensity to jam coefficient, increases with the size of the particle to gap-size ratio and, where applicable, with the value of α . No experimental data were available to back this observation. When simulating heterogeneous granular material, the CHRONO DEM-P implementation was short on accuracy and/or robustness grounds, which explains the lack of DEM-P results.

Finally, the small difference between the DEM-C flow rates for spheres ($\alpha = 1.0$) in Tables VIII and X provides an opportunity to reflect on the importance of collision detection. Indeed, in the former case, the collision detection is of sphere-to-sphere type, which has an easy-to-find analytical solution. For the latter case, the collision detection is of ellipsoid-to-ellipsoid type, a scenario that calls for the solution of an optimization problem [50]. This is despite the two ellipsoids in contact being spheres, i.e., ellipsoids with identical semiaxes. Since the optimization problem does not have an analytical solution, the collision detection is only solved approximately, which ultimately influences the simulation results.

III. CONCLUSION

The one salient conclusion of this study is that both the DEM-P and DEM-C are predictive. It is reassuring that two discrete-element methods produce similar results despite being vastly different in both their modeling and numerical solution approaches. In addition, there is no clear winner insofar as handling granular dynamics is concerned. For very large

TABLE XI. The DEM-C results for the flow rate standard deviation normalized by the flow rate \dot{m} , $\zeta = SD/\dot{m}$, for different compositions and gap sizes w (mm).

Granular composition	100ζ		
	$w = 1.5$	$w = 2.0$	$w = 2.5$
sphere ($\alpha = 1.0$)	5.6	3.6	2.1
prolate ellipsoid ($\alpha = 2.0$)	6.7	5.7	5.2
prolate ellipsoid ($\alpha = 3.0$)	19.5	9.6	6.5
prolate ellipsoid ($\alpha = 4.0$)	21.5	22.7	10.6
cube	19.6	17.2	7.5
mixture	16.3	8.1	5.6

collections of monodisperse spheres in experiments that lead to high internal stress, the DEM-P has the advantage; it is faster than the DEM-C and apt at capturing both the microscale and macroscale responses of the material. The DEM-P runs into difficulties when handling complex geometries owing to its (i) *ad hoc* approach to producing the friction and contact forces under these circumstances and (ii) sensitivity to contact information, i.e., the geometrical or collision detection component, when small variations in contact information lead to sizable changes in forces. To a point, we found the DEM-P insensitive to shearing rates, which could be increased, and to contact stiffness, which could be decreased, both by orders of magnitude. This lack of sensitivity can be traded for larger simulation step sizes that led in some experiments, e.g., the STT, to significant speed-ups over the DEM-C. The latter was very apt at handling granular material with complex element geometries when the experiment did not lead to high internal stresses. Hopper flows are very suitable, less so triaxial or other high-load shear tests. The DEM-C had two shortcomings: (a) its emphatic embrace of the rigid-body abstraction and (b) its coupled system-level solution process, which is computationally taxing. Because of (a), the DEM-C is incapable of capturing wave propagation in granular material and struggles with the STT as it cannot employ the local particle deformation mechanism that facilitates and modulates shearing in granular material. This limitation can be addressed by reverting to a finite-element method to account for grain deformation. Computationally, this is prohibitively expensive. In relation to (b), large granular dynamics problems are going to stymie the DEM-C. Moreover, the DEM-C forfeits one of its strong points since the ability to use large steps h becomes a nonfactor given the spatial and time scales on which granular dynamics takes place. The DEM-C is anticipated to be competitive in fluidized bed, particulate flow, and robotics problems in which the size of the optimization problem is small and/or the simulation can advance with large h . We found the DEM-C to be robust, which makes it permissive and forgiving. Indeed, stopping the DEM-C solution after few iterations, long before convergence, produces macroscale results that are acceptable, yet not highly accurate. This is handy in

engineering applications when the microscale behavior is of secondary interest. For instance, when designing a piece of equipment that pushes a pile of granular material, accurately resolving the microscale response of the granular material is perhaps of little concern. Instead, the priority is in producing a good overall load history that the implement acting on the granular material experiences during a work cycle. A similar situation is encountered in ground vehicle mobility analysis where, as the vehicle operates over granular terrain, the interest might be in the macroscale response only, with little concern for grain level dynamics. On a final note, it was surprising how computationally intensive both the DEM-P and DEM-C were. We had to demand tight numerical solution accuracy levels for the simulation results to come in line with experimental data. Tight accuracy translated into simulation times that were significantly longer than what we had anticipated. As a corollary, simulation results that look plausible in an animation might be far from faithfully capturing the physics at the microscale.

There are compelling reasons to believe that in the immediate future, the fully resolved DEM simulation will facilitate a significantly better understanding of complex phenomena in soft matter physics. First, the software infrastructure to carry out these simulations is predictive and becoming ubiquitous. Second, both the DEM-P and DEM-C are poised to benefit from recent substantial gains in compute power.

Disclaimer: Reference herein to any specific commercial company, product, process, or service by trade name, trademark, manufacturer, or otherwise, does not necessarily constitute or imply its endorsement, recommendation, or favoring by the United States Government or the Department of the Army (DoA). The opinions of the authors expressed herein do not necessarily state or reflect those of the United States Government or the DoA, and shall not be used for advertising or product endorsement purposes.

ACKNOWLEDGMENTS

This research was supported in part by US Army TARDEC Rapid Innovation Fund No. W56HZV-14-C-0254 and National Science Foundation Grant No. GOALI-CMMI 1362583.

-
- [1] E. J. Haug, *Computer-Aided Kinematics and Dynamics of Mechanical Systems, Volume I: Basic Methods* (Prentice Hall, Englewood Cliffs, 1989).
 - [2] A. A. Shabana, *Dynamics of Multibody Systems*, 4th ed. (Cambridge University Press, Cambridge, 2013).
 - [3] P. Richard, M. Nicodemi, R. Delannay, P. Ribiere, and D. Bideau, *Nat. Mater.* **4**, 121 (2005).
 - [4] P. Cundall, *Proc. Symp. ISRM, Nancy, France* **1**, 129 (1971).
 - [5] P. Cundall and O. Strack, *Geotechnique* **29**, 47 (1979).
 - [6] K. L. Johnson, *Contact Mechanics* (Cambridge University Press, Cambridge, 1987).
 - [7] P. Cundall, *Int. J. Rock Mech. Min. Sci. Geomech.* **25**, 107 (1988).
 - [8] H. M. Jaeger, S. R. Nagel, and R. P. Behringer, *Rev. Mod. Phys.* **68**, 1259 (1996).
 - [9] N. V. Brilliantov, F. Spahn, J.-M. Hertzsch, and T. Pöschel, *Phys. Rev. E* **53**, 5382 (1996).
 - [10] L. Vu-Quoc and X. Zhang, *Proc. R. Soc. A* **455**, 4013 (1999).
 - [11] L. Vu-Quoc, L. Lesburg, and X. Zhang, *J. Comput. Phys.* **196**, 298 (2004).
 - [12] S. Luding, in *The Physics of Granular Media*, edited by H. Hinrichsen and D. E. Wolf (Wiley-VCH Verlag GmbH, Weinheim, 2005), pp. 299–324.
 - [13] T. Pöschel and T. Schwager, *Computational Granular Dynamics: Models and Algorithms* (Springer, Berlin, 2005).
 - [14] L. E. Silbert, D. Ertas, G. S. Grest, T. C. Halsey, D. Levine, and S. J. Plimpton, *Phys. Rev. E* **64**, 051302 (2001).
 - [15] H. P. Zhang and H. A. Makse, *Phys. Rev. E* **72**, 011301 (2005).
 - [16] J. A. Fleischmann, R. Serban, D. Negrut, and P. Jayakumar, *J. Comput. Nonlin. Dyn.* **11**, 044502 (2015).

- [17] D. E. Stewart, *SIAM Rev.* **42**, 3 (2000).
- [18] D. Negrut, R. Serban, and A. Tasora, *J. Comput. Nonlin. Dyn.* (2017), doi:10.1115/1.4037415.
- [19] D. E. Stewart and J. C. Trinkle, *Int. J. Numer. Methods Eng.* **39**, 2673 (1996).
- [20] M. Anitescu, J. F. Cremer, and F. A. Potra, *Mech. Struct. Mach.* **24**, 405 (1996).
- [21] J. Trinkle, J.-S. Pang, S. Sudarsky, and G. Lo, *Z. Angew. Math. Mech.* **77**, 267 (1997).
- [22] C. Glocker and F. Pfeiffer, An LCP-approach for multibody systems with planar friction, *Proceedings of the CMIS 92 Contact Mechanics International Symposium, Lausanne, Switzerland* (CMIS, 1992), pp. 13–20.
- [23] V. Acary and B. Brogliato, *Numerical Methods for Nonsmooth Dynamical Systems: Applications in Mechanics and Electronics* (Springer, Berlin, 2008).
- [24] D. M. Kaufman and D. K. Pai, *SIAM J. Sci. Comput.* **34**, A2670 (2012).
- [25] M. Anitescu and G. D. Hart, *Int. J. Numer. Methods Eng.* **60**, 2335 (2004).
- [26] T. Heyn, M. Anitescu, A. Tasora, and D. Negrut, *Int. J. Numer. Methods Eng.* **95**, 541 (2013).
- [27] H. Mazhar, T. Heyn, A. Tasora, and D. Negrut, *ACM Trans. Graph.* **34**, 32:1 (2015).
- [28] L. Pospisil, Development of algorithms for solving minimizing problems with convex quadratic function on special convex sets and applications, Ph.D. thesis, Ostrava Technical University, 2015, available at <http://home1.vsb.cz/~pos220/>.
- [29] A. Tasora, R. Serban, H. Mazhar, A. Pazouki, D. Melanz, J. Fleischmann, M. Taylor, H. Sugiyama, and D. Negrut, Chrono: An Open Source Multi-physics Dynamics Engine, In *High Performance Computing in Science and Engineering*, edited by T. Kozubek, R. Blaheta, J. Šístek, M. Rozložník, and M. Čermák, HPCSE 2015, Lecture Notes in Computer Science Vol. 9611 (Springer, Cham, 2015), pp. 19–49.
- [30] Project CHRONO, CHRONO: An open source framework for the physics-based simulation of dynamic systems, <http://projectchrono.org>, accessed: 2016-03-07.
- [31] B. V. Derjaguin, V. M. Muller, and Y. P. Toporov, *J. Colloid Interface Sci.* **53**, 314 (1975).
- [32] K. Williams, Cone penetration results for 3mm glass beads and 20-30 Ottawa sand, Simulation-Based Engineering Laboratory, University of Wisconsin–Madison Report No. TR-2016-04, 2016, available at <http://sbel.wisc.edu/documents/TR-2016-04.pdf> (unpublished).
- [33] W. J. Likos and R. Jaafar, *J. Geotech. Geoenviron. Eng.* **140**, 04014043 (2014).
- [34] M. Kwarda and D. Negrut, Using the complementarity and penalty methods for solving frictional contact problems in Chrono: Validation for the cone penetrometer test, Simulation-Based Engineering Laboratory, University of Wisconsin–Madison Report No. TR-2016-16, 2016, available at <http://sbel.wisc.edu/documents/TR-2016-16.pdf> (unpublished).
- [35] D. J. White and W. A. Take, Cambridge University Engineering Department Report No. CUED/D-SOILS/TR322, 2002 (unpublished), http://www-civ.eng.cam.ac.uk/geotech_new/publications/TR/TR322.pdf.
- [36] M. Kwarda and D. Negrut, Using the complementarity and penalty methods for solving frictional contact problems in Chrono: Validation for the shear-test with particle image velocimetry, Simulation-Based Engineering Laboratory, University of Wisconsin–Madison Report No. TR-2016-18, 2016, available at <http://sbel.wisc.edu/documents/TR-2016-18.pdf> (unpublished).
- [37] D. Melanz, M. Hammad, and D. Negrut, A study of the effect of CCP-relaxation of the equations of motion in a differential variational inequality framework for handling frictional contact, Simulation-Based Engineering Laboratory, University of Wisconsin–Madison Report No. TR-2015-10, 2015 (unpublished).
- [38] D. Melanz, H. Mazhar, and D. Negrut, Using an anti-relaxation step to improve the accuracy of the frictional contact solution in a differential variational inequality framework for the rigid body dynamics problem, Simulation-Based Engineering Laboratory, University of Wisconsin–Madison No. TR-2016-02, 2016, available at <http://sbel.wisc.edu/documents/TR-2016-02.pdf> (unpublished).
- [39] L. Cui, C. O’Sullivan, and S. O’Neill, *Geotechnique* **57**, 831 (2007).
- [40] M. Kwarda and D. Negrut, Using the complementarity and penalty methods for solving frictional contact problems in Chrono: Validation for the triaxial test, Simulation-Based Engineering Laboratory, University of Wisconsin–Madison Report No. TR-2016-17, 2016, available at <http://sbel.wisc.edu/documents/TR-2016-17.pdf> (unpublished).
- [41] C. O’Sullivan, J. D. Bray, and M. Riemer, *J. Eng. Mech.* **130**, 1140 (2004).
- [42] L. Cui and C. O’Sullivan, *Geotechnique* **56**, 455 (2006).
- [43] H. Mazhar, T. Heyn, A. Pazouki, D. Melanz, A. Seidl, A. Bartholomew, A. Tasora, and D. Negrut, *Mech. Sci.* **4**, 49 (2013).
- [44] C. Cattaneo, *Rend. Accad. Naz. Lincei* **27**, 342 (1938).
- [45] R. D. Mindlin, *J. Appl. Mech.* **16**, A-259 (1949).
- [46] R. Mindlin and H. Deresiewicz, *J. Appl. Mech.* **20**, 327 (1953).
- [47] Y. Gonthier, J. McPhee, C. Lange, and J.-C. Piedbuf, *Multibody Syst. Dyn.* **11**, 209 (2004).
- [48] A. Roy and J. A. Carretero, *Int. J. Nonlin. Mech.* **47**, 103 (2012).
- [49] M. Boos and J. McPhee, *J. Comput. Nonlin. Dyn.* **8**, 021006 (2013).
- [50] A. Pazouki, H. Mazhar, and D. Negrut, *Math. Comput. Simul.* **82**, 879 (2012).